

Momentum-space imaging of Cooper pairing in a half-Dirac-gas topological superconductor

Su-Yang Xu¹, Nasser Alidoust¹, Ilya Belopolski¹, Anthony Richardella², Chang Liu¹, Madhab Neupane¹, Guang Bian¹, Song-Hsun Huang³, Raman Sankar³, Chen Fang^{1,4}, Brian Dellabetta⁴, Wenqing Dai², Qi Li², Matthew J. Gilbert⁴, Fangcheng Chou³, Nitin Samarth² and M. Zahid Hasan^{1,5*}

Superconductivity involving topological Dirac electrons has recently been proposed as a platform between concepts in high-energy and condensed-matter physics. It has been predicted that supersymmetry and Majorana fermions, both of which remain elusive in particle physics, may be realized through emergent particles in these particular superconducting systems. Using artificially fabricated topological-insulator-superconductor heterostructures, we present direct spectroscopic evidence for the existence of Cooper pairing in a weakly interacting half Dirac gas. Our studies reveal that two dimensional topological superconductivity in a helical Dirac gas is distinctly different from that in an ordinary two-dimensional superconductor in terms of the spin degrees of freedom of electrons. We further show that the pairing of Dirac electrons can be suppressed by time-reversal symmetry-breaking impurities, thereby removing the distinction. Our demonstration and momentum-space imaging of Cooper pairing in a half-Dirac-gas two-dimensional topological superconductor serve as a critically important platform for future testing of fundamental physics predictions such as emergent supersymmetry and topological quantum criticality.

Realization of novel superconductivity is one of the central themes in condensed matter physics in general^{1–24}. Superconductivity is a collective phenomenon, where electrons moving to the opposite directions ($\pm k$) form dynamically bound pairs, resulting in a Cooper pair gas. In an ordinary superconductor, the conduction electrons that move along a certain direction have both spin-up and spin-down electrons available for the Cooper pairing. The superconductivity observed so far, including in the conventional *s*-wave BCS superconductors as well as the cuprate or heavy fermion *d*-wave superconductors, all share this property. Recently, the discovery of 3D topological insulators (TIs) in bismuth-based semiconducting compounds has attracted much interest in condensed matter physics. In these TI materials, the bulk has a full energy gap whereas the surface exhibits an odd number of Dirac-cone electronic states, where the spin of the surface electrons is uniquely locked to their momentum^{1,2}. Therefore, at any given surface of a TI, the surface electrons moving in one direction (for example, $+k$) will have only spin-up electrons available whereas those of moving to $-k$ have only spin-down electrons available. This is in contrast to the Fermi level electronic states in an ordinary superconductor. This distinction can give rise to a wide range of exotic physics. Recently, a number of theories have highlighted these possibilities from both the fundamental physics and applications point of view^{4–10}. For example, both supersymmetry and Majorana fermions are interesting physics phenomena predicted in high-energy theories that remain unobserved in particle physics experiments. And it has been theoretically predicted, very recently, that such new physics can be realized in a condensed matter setting^{4,6}, if superconductivity can be induced in a spin-helical gas. Moreover, a low-energy realization of these phenomena can also be used to

build the topological qubit for a topological quantum computer, which therefore is also of value in device applications. The first step towards the unambiguous realization of Majorana fermions or any of the fascinating theoretical proposals requires a clear demonstration of the helical-Cooper pairing topological superconductor phase. Helical-Cooper pairing is defined as the superconducting Bose condensation of a spin-momentum-locked Dirac electron gas, independent of the bosonic character of the pairing glue^{1–3}. So far, a direct experimental demonstration of helical-Cooper pairing remains elusive.

In this paper, we use spin- and momentum-resolved photoemission spectroscopy with sufficiently high resolution and at sufficiently low temperature to allow direct evidence for the helical Cooper pairing in a spin-momentum-locked Dirac electron gas. We achieve this through the observation of the momentum-resolved Bogoliubov quasi-particle spectrum of a topological insulator (Bi_2Se_3) in proximity to a superconducting NbSe_2 substrate. We further systematically investigate the dependence of the helical Cooper pairing in the Dirac electrons on varying the TI film thickness or doping magnetic impurities. Our observation of helical-Cooper pairing and superconductivity in spin-Dirac electronic gas serves as an important platform for realizing many exotic phenomena^{1–10}. We also demonstrate a systematic methodology using the combination of spin- and momentum-resolved ARPES and interface transport that can be more generally applied to discover, isolate, and systematically optimize topological superconductivity in engineered materials.

Sample layout for Dirac superconductivity studies

High-quality $\text{Bi}_2\text{Se}_3/2\text{H-NbSe}_2$ interface heterostructures (Fig. 1a,b) are prepared using molecular beam epitaxy growth

¹Joseph Henry Laboratory, Department of Physics, Princeton University, Princeton, New Jersey 08544, USA, ²Department of Physics, The Pennsylvania State University, University Park, Pennsylvania 16802-6300, USA, ³Center for Condensed Matter Sciences, National Taiwan University, Taipei 10617, Taiwan, ⁴Department of Electrical and Computer Engineering, University of Illinois, Urbana, Illinois 61801, USA, ⁵Princeton Center for Complex Materials, Princeton Institute for Science and Technology of Materials, Princeton University, Princeton, New Jersey 08544, USA. *e-mail: mzhasan@princeton.edu

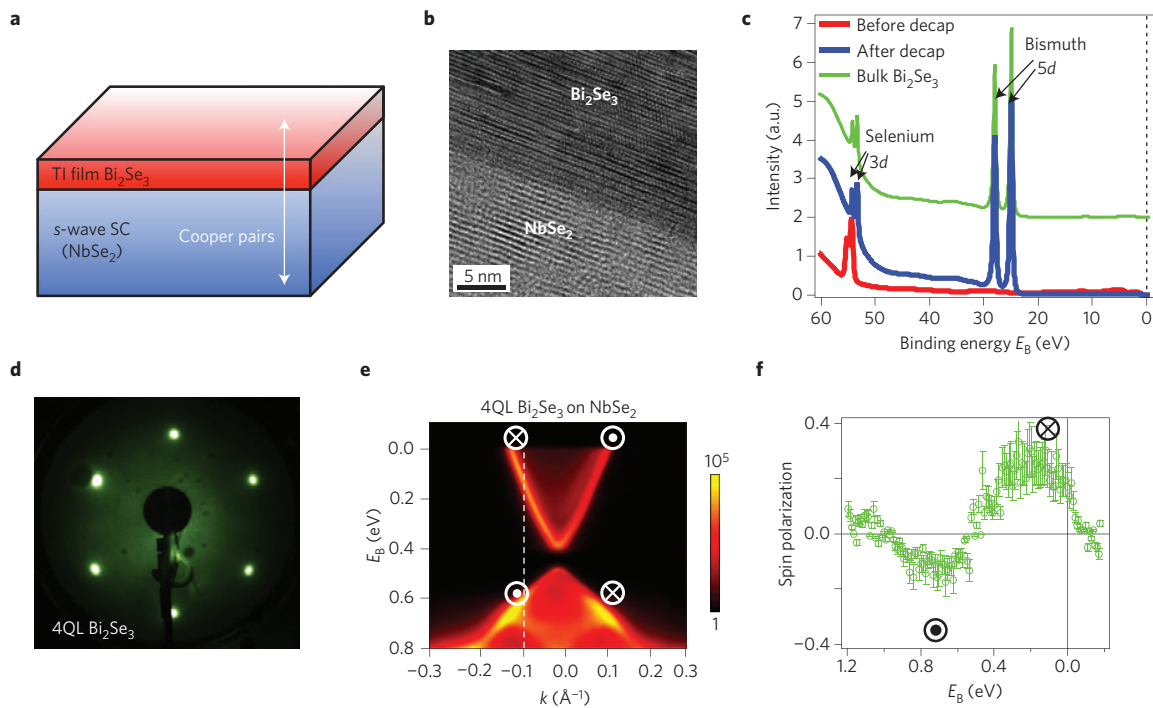


Figure 1 | Sample layout and characterization. **a**, A schematic layout of ultrathin Bi_2Se_3 films epitaxially grown on the (0001) surface of single-crystalline s -wave superconductor (SC) 2H-NbSe_2 ($T_c = 7.2$ K) using the MBE technique. **b**, High-resolution transmission electron microscopy (TEM) measurements of the $\text{Bi}_2\text{Se}_3/\text{NbSe}_2$ interface at 200 keV electron energy. An atomically abrupt transition from the NbSe_2 layered structure to the layered quintuple layer structure of Bi_2Se_3 is resolved, showing a good atomically flat interface crystal quality (see Supplementary Information B for details). **c**, Momentum-integrated ARPES intensity curves (in arbitrary units (a.u.)) over a wide binding energy window (core-level spectra) taken on a representative 3QL Bi_2Se_3 (≈ 3 nm) film grown on NbSe_2 before and after removing the amorphous selenium capping layer (decapping). **d**, A low-energy electron diffraction (LEED) image on a 4QL Bi_2Se_3 film shows a six-fold pattern, providing evidence that the thin Bi_2Se_3 film is well ordered. **e**, High-resolution ARPES dispersion map of a 4QL Bi_2Se_3 film on NbSe_2 after decapping using an incident photon energy of 50 eV. The white circle and cross schematically show the measured direction of the spin texture on the top surface of our 4QL Bi_2Se_3 film shown in **f**. A colour bar is presented on the right giving the ARPES intensity on a relative scale. **f**, Spin-resolved ARPES measurements on 4QL Bi_2Se_3 as a function of the binding energy at a fixed momentum, which is indicated by the white dotted line in **e**. The error bars show the experimental uncertainty in determining the magnitude of the spin polarization.

(MBE). The growth conditions are systematically optimized to enhance the superconductivity signals in our ARPES measurements. To protect the Bi_2Se_3 surface from exposure to atmosphere, an amorphous selenium layer is deposited on top of the TI surface. This layer can be removed *in situ* in our angle-resolved photoemission spectroscopy (ARPES) experiments by annealing the samples, as demonstrated in Fig. 1c,d (see Supplementary Information A.1 and also ref. 25 for details). High-resolution ARPES measurements on the Bi_2Se_3 surface are then performed (Fig. 1e). A sharp spectrum for the Dirac surface states is clearly observed, indicating the good surface/interface quality of our heterostructure. Furthermore, we perform spin-resolved ARPES measurements (photon energy 50 eV) on the 4-quintuple-layer (QL) sample (Fig. 1f). At the Fermi level, a left-handed spin-momentum-locking profile is observed, which is one of the critical ingredients for the helical-Cooper pairing, as we will show in later sections. In Supplementary Information C, we further present comprehensive spin-resolved measurements and demonstrate reliability.

Pairing gap in helical surface states

Figure 2a shows the ARPES dispersion maps of the Bi_2Se_3 films with different thicknesses grown on NbSe_2 . We start with the 4QL sample using an incident photon energy of 18 eV, as shown in Fig. 2b. Six representative momenta, namely $\pm\hbar k_1$, $\pm\hbar k_2$ and $\pm\hbar k_3$ are chosen for detailed studies, where $k_1 = 0.12 \text{ \AA}^{-1}$ corresponds to the topological surface states (TSSs), and $k_2 = 0.08 \text{ \AA}^{-1}$ and $k_3 = 0.04 \text{ \AA}^{-1}$ correspond to the outer and inner parts of the bulk band states,

respectively. Figure 2c shows the ARPES spectra at a momentum of k_1 (TSSs) at different temperatures. Clear leading-edge shifts (superconducting gap) and coherence peaks are observed at low temperatures. The observed superconducting signals as temperature increases disappear at higher temperatures such as $T = 7$ K and 12 K. To better visualize the superconductivity gap in our data, the ARPES spectra are symmetrized with respect to the Fermi level, where the temperature evolution of the full (symmetrized) superconducting gap and the coherence peaks are clearly seen in Fig. 2d. These measurements show the existence of induced superconductivity in the helical Dirac electrons occurring in the Bi_2Se_3 TSSs, which is not possible in conventional momentum-integrated experiments that lack spin resolution^{11–20}. We compare and contrast the proximity-induced superconductivity in the Dirac surface states to that of the bulk band states, as shown in Fig. 2e. To obtain the magnitude of the superconducting energy gap (shown in Fig. 2f), we fit the bulk state ($\pm\hbar k_2$, and $\pm\hbar k_3$) data by the Dynes function²⁶ (black curves in Fig. 2g), which is widely used in s -wave superconductors, whereas the surface state data ($\pm\hbar k_1$) is fitted by a BCS function taking into account the spin-momentum-locking and Dirac dispersion properties of the TSSs (blue curves in Fig. 2g). To further isolate the signals of Dirac surface states from the bulk bands, we choose another incident photon energy of 50 eV (Fig. 2h), where we use the photoemission matrix element effect to suppress the spectral weight of the bulk conduction states. We subsequently study the spectra at momentum k_1 where the ARPES signal is dominated by the contribution from the surface states. Leading-edge shifts

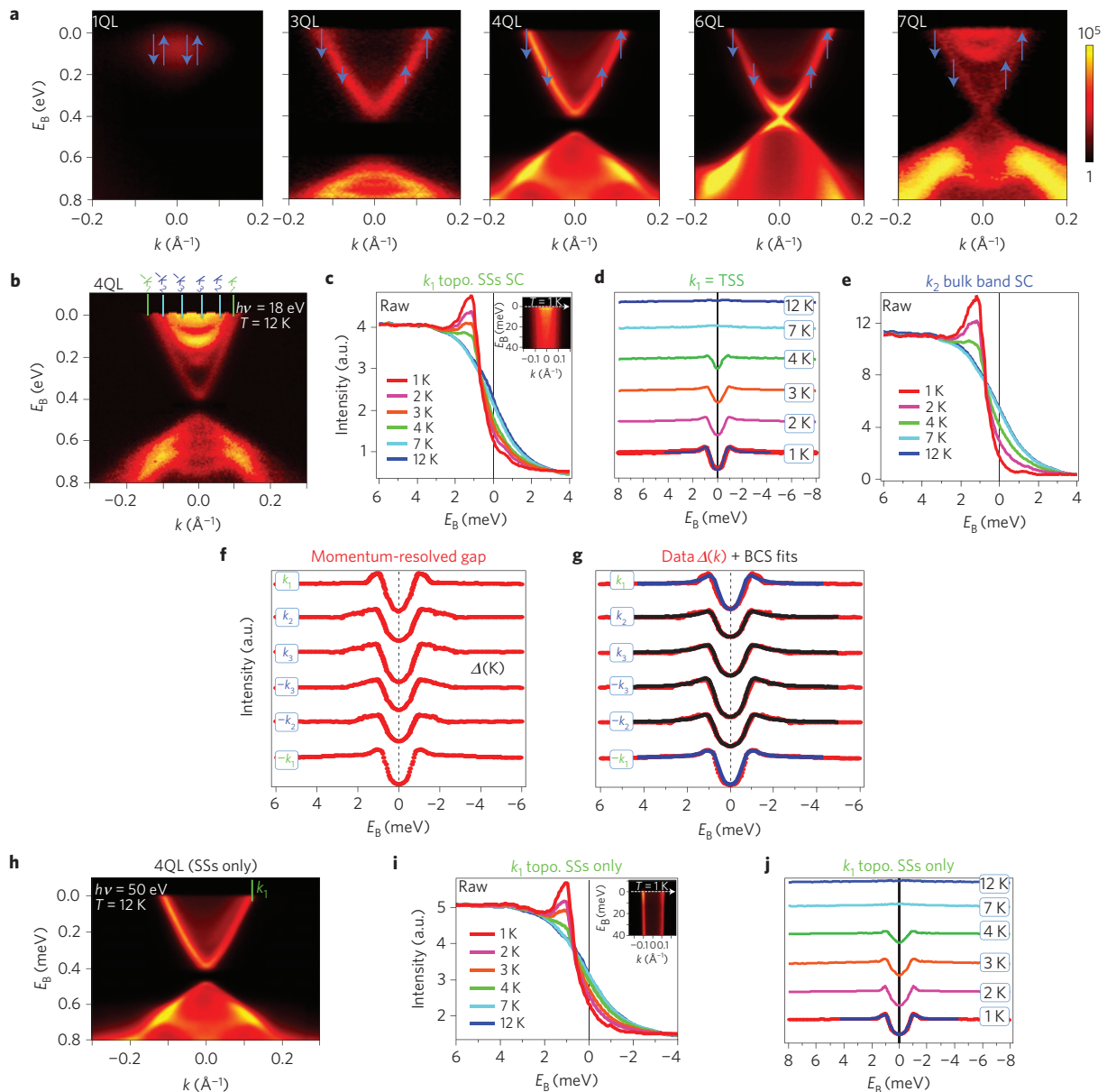


Figure 2 | Spectroscopically resolved proximity-induced topological superconductivity. **a**, ARPES dispersion maps of Bi₂Se₃/NbSe₂ as a function of Bi₂Se₃ film thickness. The blue arrows quantitatively depict the spin texture configuration in the ultrathin limit. The length of the arrow is proportional to the magnitude of the spin polarization. **b**, ARPES dispersion map of a 4QL Bi₂Se₃ film measured at $T = 12$ K using an incident photon energy of 18 eV. **c**, ARPES spectra at fixed momentum k_1 (the topological surface states). **d**, Symmetrized ARPES spectra at fixed momentum k_1 . **e**, ARPES spectra at fixed momentum k_2 (bulk band states). **f, g**, Symmetrized ARPES spectra at $\pm k_1$, $\pm k_2$ and $\pm k_3$ at $T \sim 1$ K (**f**). The surface state gap ($\pm k_1$) is further fitted (blue curves) by a BCS function taking into account its spin-momentum-locking and Dirac dispersion properties (Supplementary Information A), whereas the bulk gap is fitted (black curves) by the Dynes function²⁶ (**g**). **h**, ARPES dispersion map of a 4QL Bi₂Se₃ film measured with an incident photon energy of 50 eV. **i, j**, ARPES spectra (**i**) and symmetrized ARPES spectra (**j**) at fixed momentum k_1 . The insets of **c, i** show an ARPES dispersion map near the Fermi level at a low temperature of $T \sim 1$ K at photon energies of 18 eV and 50 eV, respectively.

and coherence peaks (Fig. 2i,j) are clearly observed from k_1 , which confirms the superconductivity in the Dirac surface states using a different photon energy. In Supplementary Information F.4.1, we present additional data and analysis to further exclude extrinsic possibilities or artefacts.

We perform ARPES measurements around the surface state Fermi surface as a function of Fermi surface azimuthal angle θ , to study the extent of anisotropy of the surface state superconducting gap. Five representative momentum-space cut-directions ($\theta_1 - \theta_5$) are chosen, as indicated by the dotted lines in Fig. 3a. The helical-surface state superconducting gap observed by ARPES at different

θ angles and their fits are shown in Fig. 3b. The reasonably good surface state fitting results (blue curves in Figs 2g and 3b) indicate that the obtained surface state superconductivity is consistent with its spin-helical and linear dispersive properties, which supports its helical-Cooper pairing nature. The obtained magnitude of the superconducting order parameter is then plotted as a function of Fermi surface angle in Fig. 3c. The superconducting gap is found to be nearly isotropic, which is also consistent with the time-reversal-invariant helical nature of the surface state superconductivity as expected theoretically^{6,7}. We note that although helical Cooper pairing can also occur in other 2D systems with spin-polarized

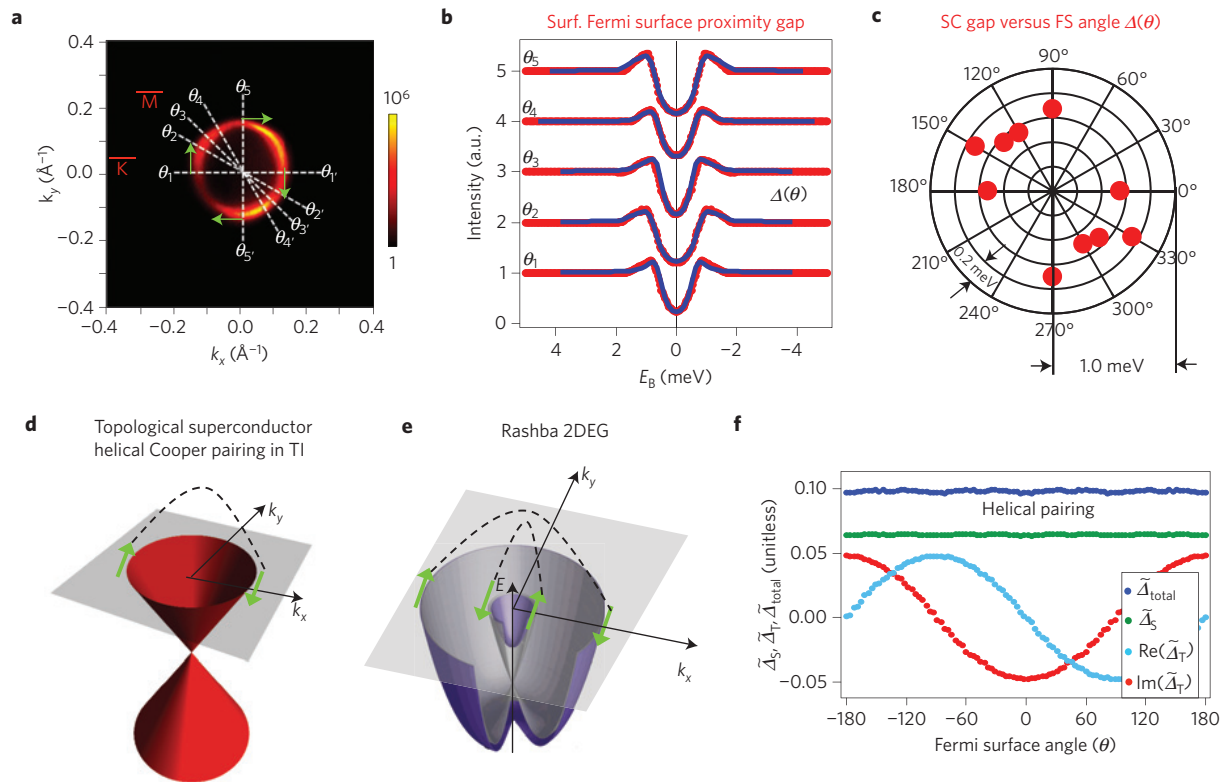


Figure 3 | Topological superconducting gap and helical Cooper pairing. **a**, Fermi surface map taken at an incident photon energy of 50 eV. The white dotted lines indicate the momentum-space cut-directions chosen to study the surface state superconducting gap as a function of Fermi surface angle θ around the surface state Fermi surface. **b**, Symmetrized and normalized ARPES spectra along θ_1 through θ_5 respectively (red) and their surface gap fittings. **c**, Fermi surface angle dependence of the estimated superconducting gap around the surface state Fermi surface. **d**, Illustrations depicting helical-Cooper pairing in a spin-momentum-locked helical electron gas. There is only one (an odd number of) helical Cooper pairing channel(s) for the single Dirac-cone surface states per Brillouin zone in a TI. **e**, Helical Cooper pairing can also occur in other 2D systems with spin-polarized bands, such as a Rashba 2DEG, but a key distinction is that in a Rashba 2DEG there are two (an even number of) channels for helical Cooper pairing per Brillouin zone (the helical Cooper pairing within the inner and the outer Fermi surface, respectively). The arrows in **d,e** show the direction of the spin polarization of the electrons at the Fermi level. **f**, Model calculation results of a topological insulator film in proximity to an s-wave superconductor (see Supplementary Information D.2 for more details) show the calculated total superconducting pairing amplitude and its decomposed singlet ($\tilde{\Delta}_S$) and triplet ($\tilde{\Delta}_T$) components on the top surface of a four-unit-cell-thick TI interfaced with an s-wave superconductor, which further confirms the helical (topologically nontrivial) nature of the induced surface state superconductivity in our Bi_2Se_3 films. Because $\tilde{\Delta}$ is a dimensionless number (see Supplementary Information D for discussion), we use a tilde in $\tilde{\Delta}$ to differentiate it from the superconducting gap Δ measured in the experiments.

bands, such as a Rashba 2DEG, a key distinction is that in a Rashba 2DEG there are two channels (an even number) for helical Cooper pairing per Brillouin zone (the helical Cooper pairing within the inner and the outer Fermi surfaces, respectively, see Fig. 3e). In contrast, in the system considered in this work, there is only one channel (an odd number) for helical Cooper pairing (the single channel provided by the Dirac surface states, Fig. 3d). The odd number of helical Cooper pairing channels, as demonstrated here, is indispensable for many fascinating phenomena predicted in theory^{4–10}. In Fig. 3f and Supplementary Information D, we present model calculation analysis, which shows a $p_x \pm ip_y$ superconducting order parameter in the Dirac surface states, supporting the helical Cooper pairing nature. Therefore, through our systematic ARPES measurements with simultaneous energy, momentum and spin resolution, we observe superconductivity in an odd number of spin-momentum-locked Dirac surface states, which serves as direct experimental evidence for helical-Cooper pairing.

Surface-surface hybridization and magnetic doping

We study the observed superconductivity in the surface states as a function of surface-to-surface hybridization strength (effectively as a function of the TI film thickness), to experimentally prove

its proximity-induced nature. As shown in Fig. 4a, a sample with a Dirac point hybridization gap as large as ~ 200 meV is realized in a 3QL film sample. Clear leading-edge shifts, coherence peaks and their temperature evolution are observed in the TSSs near the Fermi energy (Fig. 4b,c), evidence for helical-Cooper pairing and helical superconductivity in the 3QL film samples. The observed surface state superconducting gap value is about 0.7–0.8 meV. We now turn to a gapless (7QL) sample, as shown in Fig. 4d. The absence of hybridization gap at the Dirac point reveals that surface state wavefunctions from the top and the interface surfaces are completely separated in real space^{25,27,28}. Finite superconductivity signals are observed in the ARPES spectra both at momenta of k_1 (Dirac surface states) and k_2 (bulk conduction states), which are found to be weaker than the gapped samples (Fig. 4e,f). The Bi_2Se_3 top surface's superconducting gap as a function of Dirac point gap value (surface-to-surface hybridization strength) is shown in Fig. 4g,h in a (surface and bulk) band-resolved fashion. It can be seen that the induced superconducting gap near the top surface increases with a larger hybridization gap, which is realized in thinner TI films. This observation is qualitatively consistent with the theoretical description of the superconducting proximity effect, where the Cooper pair potential on the top surface is

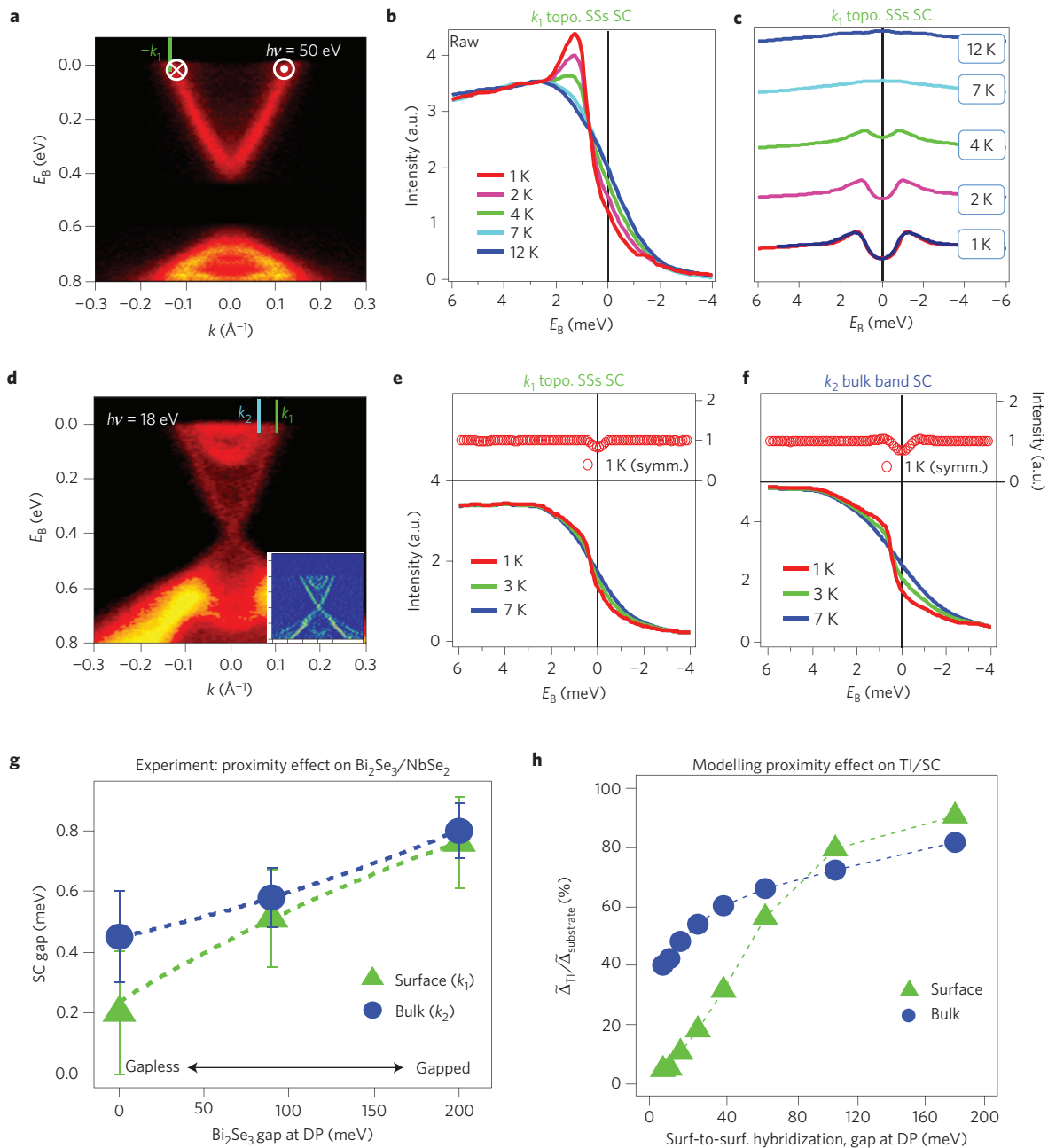


Figure 4 | Hybridization dependence of the superconducting gap. **a**, ARPES dispersion map of a 3QL Bi₂Se₃ film measured at $T = 12$ K using an incident photon energy of 50 eV. **b**, ARPES spectra at fixed momentum k_1 at different temperatures. **c**, Symmetrized ARPES spectra at different temperatures. **d**, ARPES dispersion map of a 7QL Bi₂Se₃ film measured at $T = 12$ K using an incident photon energy of 18 eV. The inset shows a second derivative image of the ARPES dispersion map. **e, f**, ARPES spectra at fixed momenta k_1 (surface states (**e**)) and k_2 (bulk states (**f**)). **g**, ARPES-measured superconducting gap for topological surface states (k_1) and for the bulk conduction states (k_2) as a function of the Dirac point gap value (surface-to-surface hybridization strength). The dotted lines are guides to the eye. The error bars here show the uncertainty in determining the superconducting gap via fitting the ARPES spectra. **h**, Calculated dependence on surface-to-surface hybridization. Because the pairing amplitude $\tilde{\Delta}_{\text{TI}}$ in the calculation is a dimensionless number, we normalize it by the pairing amplitude of the substrate superconductor, $\tilde{\Delta}_{\text{substrate}}$ (a constant).

enhanced with the decreasing thickness of the normal metal. More interestingly, it can be seen that the surface state superconducting gap increases at a faster rate than that of the proximity gap on the bulk band. Such a contrast reveals that stronger surface-to-surface hybridization significantly enhances the helical pairing in the surface states on the top surface. These fine details of the superconducting proximity effect observed in our data will be a valuable guide in properly interpreting the vast complexity of the transport data addressing the proximity effects in TI films and

heterostructures. In Supplementary Information A.5, we further present our ARPES data on magnetically (Mn) doped Bi₂Se₃ grown on top of NbSe₂, where we show that magnetic impurities lead to strong pair-breaking in both conventional (bulk) and helical (surface) pairing channels. By showing that the superconducting gap in the surface states decreases in the presence of magnetic dopants (Supplementary Information A.5), we have provided an important check for our main result that we have observed Cooper pairing in the surface states. Therefore, our measurements have

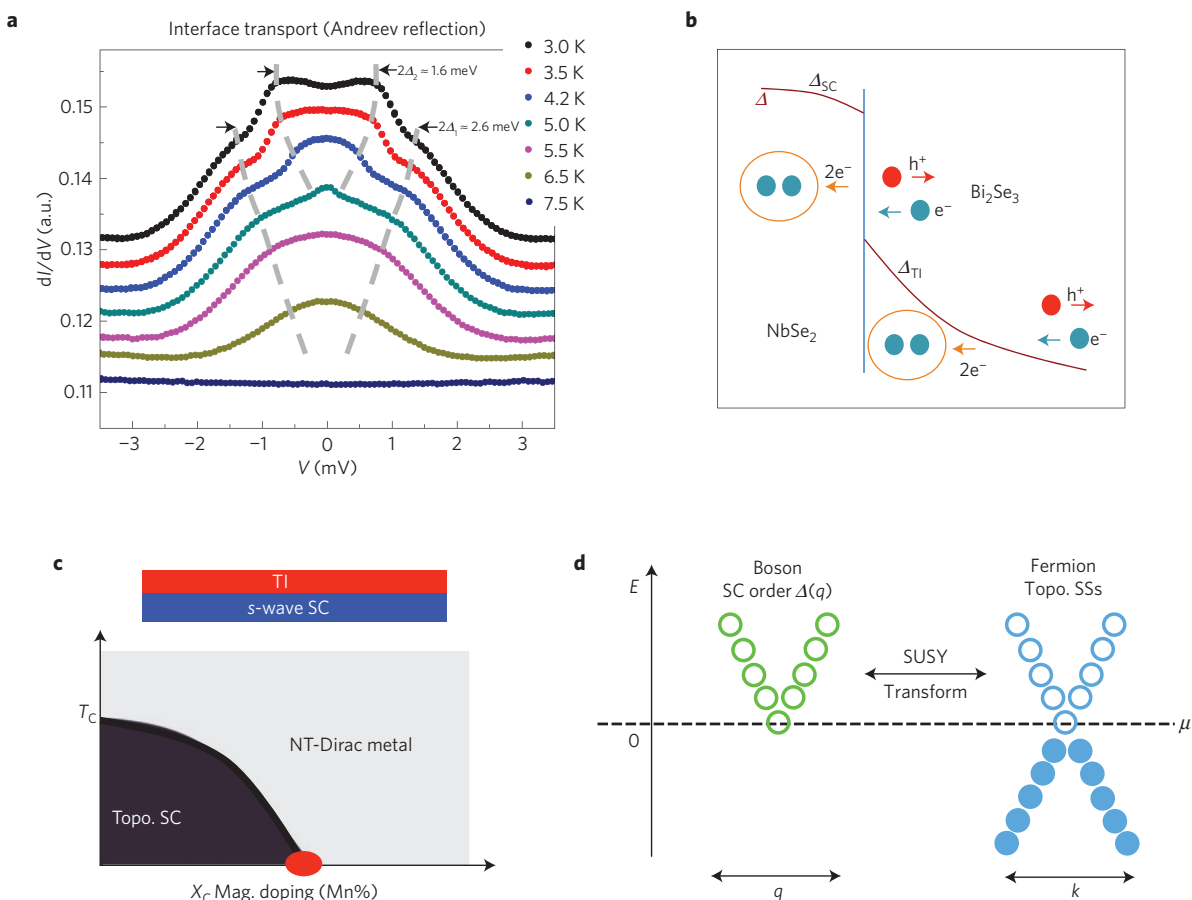


Figure 5 | Point-contact interface transport and conditions for predicted emergent supersymmetry. **a**, Point-contact transport (dI/dV versus bias voltage) as a function of temperature. For $T = 3.5$ K, below the T_c of NbSe_2 , as the bias voltage is swept from ± 3 mV to 0 mV, dI/dV first increases, then levels off at $|V| \simeq 1.3$ mV, and then increases again, reaching a maximum at $|V| \simeq 0.8$ mV. dI/dV for other $T < T_c$ exhibits a similar behaviour. This indicates two Andreev-reflection channels with different sizes of superconducting gap. **b**, The two Andreev-reflection processes via the induced superconducting gap in Bi_2Se_3 and intrinsic superconducting gap in NbSe_2 , respectively. e^- and h^+ represent electrons and holes that are involved in the Andreev-reflection process. **c,d**, Theoretically proposed⁴ unusual criticality related to supersymmetry phenomena can be realized in the topological insulator/s-wave superconductor interface as the chemical potential is tuned to the surface state Dirac point and an in-plane magnetization drives the system to the critical point between superconducting and normal non-topological (NT) Dirac metal phases (schematically shown in **c**). Fermions and bosons are expected to feature the same band velocity and quasi-particle lifetime⁴ (schematically shown in **d**), where the fermion velocity is estimated to be around $5 \times 10^5 \text{ m s}^{-1}$ from our ARPES result. This cartoon refers to a future possibility.

identified two ways to suppress the helical Cooper pairing near the top surface of the Bi_2Se_3 film away from the TI/SC interface: increasing film thickness or doping with time-reversal-breaking magnetic elements.

Point-contact Andreev-reflection transport

To check that the top surface superconductivity is indeed a proximity effect, we use the well-established methodology of point-contact Andreev-reflection measurements to compare the induced gap values at the $\text{NbSe}_2/\text{Bi}_2\text{Se}_3$ heterointerface. The point contact probe is characterized by measurements on pure NbSe_2 (ref. 29) (shown in Supplementary Information E.1). The point-contact spectra on a $\text{NbSe}_2/\text{Bi}_2\text{Se}_3$ (16QL) heterostructure sample are shown in Fig. 5a,b. At temperatures below the T_c (~ 7.2 K) of NbSe_2 , the differential conductance (dI/dV) around zero bias increases as a result of the Andreev-reflection process, similar to the bare NbSe_2 spectra. Interestingly, a second differential conductance increase appears below ~ 5 K. The sharp rise of differential conductance corresponds to the energy gap of the superconducting layer. From the data, we obtain the larger gap (Δ_1) changing from 0 to 1.3 ± 0.2 mV from 7.5 K to 3.0 K. The

second gap (Δ_2) feature changes from 0 to 0.8 ± 0.2 mV from 5.0 K to 3.0 K (See Supplementary Information E.2 for more details). Injected electrons from the point-contact are Andreev-reflected inside the superconducting Bi_2Se_3 proximity layer if their energies are lower than the induced superconducting gap in Bi_2Se_3 . When their energies are above the induced gap Δ_{TI} but below the NbSe_2 superconducting gap Δ_{SC} , injected electrons are not affected by the order parameter in the Bi_2Se_3 layer but Andreev-reflected in the NbSe_2 region. Therefore, the edge around Δ_1 is probably due to the NbSe_2 gap, whereas the sharp edge around Δ_2 in the conductance spectrum probably reflects the induced gap in Bi_2Se_3 near the interface. It is worth noting that, unlike ARPES, which is mostly sensitive to the top surface, the point-contact transport probes deeper into the superconductor, similar to the electron mean free path, which is estimated to be ~ 16 nm in our films (see Supplementary Information E.2 for more details). Our results thus suggest that the combination of ARPES and point-contact transport together provides a powerful method for probing superconducting proximity effects which can be used to correlate the proximity gap on the top surface and the buried interface if film thickness is not too large (not larger than the superconducting coherence length).

Discussions

In contrast to idealized theoretical models^{6,7} of topological superconductivity where only Dirac surface states cross the Fermi level, real samples exhibit a complex phenomenology due to the coexistence of multiple bands at the chemical potential, as demonstrated in our data above. Thus, the interpretation of experimental studies must take into account both the desirable Cooper pairing from the Dirac surface states and conventional superconductivity from the bulk, trivial surface states and impurity surface states. The coexistence of multiple bands at the Fermi level means that any superconductivity realized in actual TI materials consists of not only the desirable helical Cooper pairing from the Dirac surface states, but also conventional superconductivity from the bulk states, as shown above in our data. We note that, although progress has been reported by using conventional transport and STM experiments^{11–20}, those studies do not have the spin and momentum resolution necessary to distinguish helical Cooper pairing from that of the conventional superconductivity from other bands that intermix at the interface, making the interpretation of Majorana fermions unreliable or complex. Hence a direct experimental demonstration of the existence of superconductivity in the helical Cooper pairing channel remained elusive before our momentum and spin space observations reported here. In fact, it has been recently shown, both theoretically and experimentally^{21–24}, that the conventional superconductivity in the bulk and impurity bands at the interface or surface lead to ambiguous interpretations of the transport and STM data. To achieve a clear case for a Majorana zero mode, the helical component of the Cooper pairing must be isolated, as demonstrated here. Therefore, it is in this context that our observation of helical Cooper pairing and superconductivity in a half Dirac gas is of critical importance. Furthermore, the overall methodology employed here can be applied to isolate helical Cooper pairing in other systems and, in connection to a feedback loop, for material growth for the optimization of the helical channel. We also note that our systematic studies (by observing the superconducting gap (leading-edge shift), the clear coherence peak, as well as their systematic dependence on varying temperature, TI film thickness and doping magnetic impurities) identify the helical Cooper pairing and topological superconductivity in the TI Dirac surface states. This is in contrast to the ARPES results on Bi₂Se₃/BSCCO samples^{30–32}. Thus, our data strongly supports the view that TI/NbSe₂ is a more ideal platform than TI/BSCCO for the proposed novel physics if the system can be further optimized to increase the helical Cooper pairing channel by tuning the material parameters.

We discuss one of the interesting phenomena—the condensed matter supersymmetry—which can be enabled by our identification of a topological superconductor with helical-Cooper pairing³⁵. As shown in Fig. 5c,d, magnetic doping or an external in-plane magnetic field is necessary to drive the system to the critical point between the helical superconductivity and the normal Dirac gas states, with the chemical potential tuned to the Dirac point (demonstrated in Supplementary Information A.4). Under this condition, theory predicts that topological surface states (a fermionic excitation) and the fluctuations of superconducting order (a bosonic excitation) satisfy a supersymmetry relationship, and therefore, strikingly, possess the same Fermi/Dirac velocity and the same lifetime or self-energy⁴. We note that our present data do not provide evidence for supersymmetry, but this is an exciting future direction that we hope to access thanks to our identification of the helical-Cooper pairing and its magnetic doping response. Although the superpartners of elementary particles in high-energy physics have never been experimentally observed, the experimental methodologies, artificial sample fabrication control and experimental observations reported here pave the way for simulating and testing high-energy physics concepts in a solid-state chip³⁵.

Methods

Single-crystalline 2H-NbSe₂ samples (~3 mm × 3 mm) were grown using the iodine vapour transport method³³, where a high residual resistivity ratio (RRR = $\rho_{300\text{K}}/\rho_{0\text{K}} \sim 100$) was achieved. The NbSe₂ crystals were cleaved *in situ* under ultrahigh vacuum, and high-quality topological insulator Bi₂Se₃ thin films were then grown on top of freshly cleaved surfaces of NbSe₂ crystals using standard MBE methods (Supplementary Information B).

Ultralow temperature and ultrahigh energy resolution ARPES measurements were performed using the UE112-lowE-PGM-b+1³ ARPES beamline in the BESSY II storage ring in Berlin, Germany, which was equipped with a VG Scienta 4000 electron analyser and ³He cryo-manipulator, using an incident photon energy range from 17 eV to 80 eV, with the lowest achievable sample temperature of about 0.9 K and a base pressure of $<5 \times 10^{-11}$ torr. The total energy and momentum resolution were set to ~ 2.4 meV and 0.01 \AA^{-1} . Spin-resolved ARPES measurements were performed with linearly *p*-polarized light at synchrotron radiation photon energies from 50 eV to 70 eV, where the final state effects have been demonstrated to be negligible³⁴. Further ARPES measurements characterizing the overall electronic structure of Bi₂Se₃/NbSe₂ (including NO₂ adsorption experiments) were also performed with 29–64 eV incident photon energies at beamlines 4.0.3, 10.0.1 and 12.0.1 at the Advanced Light Source (ALS) in the Lawrence Berkeley National Laboratory (LBNL) in Berkeley, and with a 10–30 eV incident photon energy range at beamline 5–4 of the Stanford Synchrotron Radiation Lightsource (SSRL) in the Stanford Linear Accelerator Center (SLAC) Laboratory in Menlo Park. The base temperature and base pressure of the ARPES beamlines at the ALS and the SSRL were about 15 K and $<5 \times 10^{-11}$ torr, and the total energy and momentum resolution of these beamlines were about 10–15 meV and 0.01 \AA^{-1} , respectively.

Received 4 June 2014; accepted 22 September 2014;
published online 2 November 2014

References

- Hasan, M. Z. & Kane, C. L. Topological insulators. *Rev. Mod. Phys.* **82**, 3045–3067 (2010).
- Qi, X.-L. & Zhang, S.-C. Topological insulators and superconductors. *Rev. Mod. Phys.* **83**, 1057–1110 (2011).
- Wray, L. A. *et al.* Observation of topological order in a superconducting doped topological insulator. *Nature Phys.* **6**, 855–859 (2010).
- Grover, T., Sheng, D. N. & Vishwanath, A. Emergent space-time supersymmetry at the boundary of a topological phase. *Science* **344**, 280–283 (2014).
- Nandkishore, R., Levitov, L. S. & Chubukov, A. V. Chiral superconductivity from repulsive interactions in doped graphene. *Nature Phys.* **8**, 158–163 (2012).
- Fu, L. & Kane, C. L. Superconducting proximity effect and Majorana fermions at the surface of a topological insulator. *Phys. Rev. Lett.* **100**, 096407 (2008).
- Qi, X.-L., Hughes, T. L., Raghu, S. & Zhang, S.-C. Time-reversal-invariant topological superconductors and superfluids in two and three dimensions. *Phys. Rev. Lett.* **102**, 187001 (2009).
- Potter, A. C. & Lee, P. A. Engineering a *p+ip* superconductor: Comparison of topological insulator and Rashba spin-orbit-coupled materials. *Phys. Rev. B* **83**, 184520 (2011).
- Sau, J. D. *et al.* A generic new platform for topological quantum computation using semiconductor heterostructures. *Phys. Rev. Lett.* **104**, 040502 (2010).
- Hosur, P. *et al.* Majorana modes at the ends of superconductor vortices in doped topological insulators. *Phys. Rev. Lett.* **107**, 097001 (2011).
- Hor, Y. S. *et al.* Superconductivity in Cu_xBi₂Se₃ and its implications for pairing in the undoped topological insulator. *Phys. Rev. Lett.* **104**, 057001 (2010).
- Sasaki, S. *et al.* Topological superconductivity in Cu_xBi₂Se₃. *Phys. Rev. Lett.* **107**, 217001 (2011).
- Zhang, D. *et al.* Superconducting proximity effect and possible evidence for Pearl vortices in a candidate topological insulator. *Phys. Rev. B* **84**, 165120 (2011).
- Koren, G. *et al.* Proximity-induced superconductivity in topological Bi₂Te₂Se and Bi₂Se₃ films: Robust zero-energy bound state possibly due to Majorana fermions. *Phys. Rev. B* **84**, 224521 (2011).
- Sacépé, B. *et al.* Gate-tuned normal and superconducting transport at the surface of a topological insulator. *Nature Commun.* **2**, 575 (2011).
- Qu, F. *et al.* Strong superconducting proximity effect in Pb–Bi₂Te₃ hybrid structures. *Sci. Rep.* **2**, 339 (2012).
- Cho, S. *et al.* Symmetry protected Josephson supercurrents in three-dimensional topological insulators. *Nature Commun.* **4**, 1689 (2013).
- Williams, J. R. *et al.* Unconventional Josephson effect in hybrid superconductor–topological insulator devices. *Phys. Rev. Lett.* **109**, 056803 (2012).
- Xu, J.-P. *et al.* Artificial topological superconductor by the proximity effect. *Phys. Rev. Lett.* **112**, 217001 (2014).

20. Mourik, V. *et al.* Signatures of Majorana fermions in hybrid superconductor–semiconductor nanowire devices. *Science* **336**, 1003–1007 (2012).
21. Liu, J. *et al.* Zero-bias peaks in the tunneling conductance of spin–orbit-coupled superconducting wires with and without Majorana end-states. *Phys. Rev. Lett.* **109**, 267002 (2012).
22. Roy, D., Bondyopadhyaya, N. & Tewari, S. Topologically trivial zero-bias conductance peak in semiconductor Majorana wires from boundary effects. *Phys. Rev. B* **88**, 020502(R) (2013).
23. Churchill, H. O. H. *et al.* Superconductor–nanowire devices from tunneling to the multichannel regime: Zero-bias oscillations and magnetoconductance crossover. *Phys. Rev. B* **87**, 241401(R) (2013).
24. Lee, E. J. H. *et al.* Spin-resolved Andreev levels and parity crossings in hybrid superconductor–semiconductor nanostructures. *Nature Nanotech.* **9**, 79–84 (2014).
25. Xu, S.-Y. *et al.* Hedgehog spin texture and Berry's phase tuning in a magnetic topological insulator. *Nature Phys.* **8**, 616–622 (2012).
26. Okazaki, K. *et al.* Octet-line node structure of superconducting order parameter in KFe_2As_2 . *Science* **337**, 1314–1317 (2012).
27. Zhang, Y. *et al.* Crossover of the three-dimensional topological insulator Bi_2Se_3 to the two-dimensional limit. *Nature Phys.* **6**, 584–588 (2010).
28. Neupane, M. *et al.* Observation of quantum-tunneling modulated spin texture in ultrathin topological insulator Bi_2Se_3 Films. *Nature Commun.* **5**, 4841 (2014).
29. Blonder, G., Tinkham, M. & Klapwijk, T. Transition from metallic to tunneling regimes in superconducting microconstrictions: Excess current, charge imbalance, and supercurrent conversion. *Phys. Rev. B* **25**, 4515–4532 (1982).
30. Wang, E. *et al.* Fully gapped topological surface states in Bi_2Se_3 films induced by a *d*-wave high-temperature superconductor. *Nature Phys.* **9**, 621–625 (2013).
31. Xu, S.-Y. *et al.* Fermi-level electronic structure of a topological-insulator/cuprate-superconductor based heterostructure in the superconducting proximity effect regime. *Phys. Rev. B* **90**, 085128 (2014).
32. Yilmaz, T. *et al.* Absence of a proximity effect in a topological insulator on a cuprate superconductor: $\text{Bi}_2\text{Se}_3/\text{Bi}_2\text{Sr}_2\text{CaCu}_2\text{O}_8$. *Phys. Rev. Lett.* **113**, 067003 (2014).
33. Iwaya, K. *et al.* Electronic state of NbSe_2 investigated by STM/STS. *Physica B* **329–333**, 1598–1599 (2003).
34. Sánchez-Barriga, J. *et al.* Photoemission of Bi_2Se_3 with circularly polarized light: Probe of spin polarization or means for spin manipulation? *Phys. Rev. X* **4**, 011046 (2014).
35. Hasan, M. Z. *Topological Insulators: A New State of Quantum Matter presentation at Nobel Symposium on New Forms of Matter* <http://www.fysik.su.se/~ardonne/nobel/ns156-program.pdf> (2014).

Acknowledgements

The work at Princeton and Princeton-led synchrotron-based ARPES measurements is supported by US DOE DE-FG-02-05ER46200. MBE growth of $\text{Bi}_2\text{Se}_3/\text{NbSe}_2$ samples at Penn State was supported by ARO through ARO-MURI (W911NF-12-1-0461). The point-contact measurements were supported by US DOE DE-FG02-08ER4653 (Q.L.). C.F. and M.J.G. are supported by the ONR under grant N00014-11-1-0728 and N00014-14-1-0123 and B.D. and M.J.G. are supported by the AFOSR under grant FA9550-10-1-0459. Initial materials work was supported by MRSEC Program Grant DMR-0819860. M.J.G. is supported by NSF CAREER Award ECCS 13-51871. F.C.C. acknowledges the support provided by MOST-Taiwan under project number NSC-102-2119-M-002-004. We gratefully acknowledge E. Rienks for assistance at the BESSY facility. We also thank J. Denlinger, S.-k. Mo, A. Fedorov, and M. Hashimoto for beamline support at the beamlines 4.0.3, 10.0.1, 12.0.1 at the ALS, and the beamline 5–4 at the SSRL, respectively.

Author contributions

S.-Y.X., N.A., I.B., C.L., M.N., and G.B. conducted the ARPES experiments with the assistance from M.Z.H.; A.R. and N.S. performed the Bi_2Se_3 MBE growth; S.-H.H., R.S., and F.C. prepared the NbSe_2 single crystalline samples; W.D. and Q.L. conducted the point-contact Andreev-reflection transport measurements; C.F., B.D., and M.J.G. performed theoretical calculations. M.Z.H. was responsible for the conception, overall direction, planning and integration among the research units.

Additional information

Supplementary information is available in the [online version of the paper](#). Reprints and permissions information is available online at www.nature.com/reprints. Correspondence and requests for materials should be addressed to M.Z.H.

Competing financial interests

The authors declare no competing financial interests.